Facile Synthesis of Hematite Quantum-Dot/Functionalized Graphene-Sheet Composites as Advanced Anode Materials for Asymmetric Supercapacitors

8 AUTHORS, INCLUDING:

Hui Xia
Nanjing University of Science and Technology
91 PUBLICATIONS **2,343** CITATIONS

SEE PROFILE

Bin Zhao
Nanjing University
25 PUBLICATIONS **239** CITATIONS

SEE PROFILE

Zixia Lin
Nanjing University
19 PUBLICATIONS **128** CITATIONS

SEE PROFILE

Serguei Savilov
Lomonosov Moscow State University
12 PUBLICATIONS **32** CITATIONS

SEE PROFILE

Facile Synthesis of Hematite Quantum-Dot/Functionalized Graphene-Sheet Composites as Advanced Anode Materials for Asymmetric Supercapacitors

Hui Xia,* Caiyun Hong, Bo Li, Bin Zhao, Zixia Lin, Mingbo Zheng,* Serguei V. Savilov, and Serguei M. Aldoshin

For building high-energy density asymmetric supercapacitors, developing anode materials with large specific capacitance remains a great challenge. Although Fe_2O_3 has been considered as a promising anode material for asymmetric supercapacitors, the specific capacitance of the Fe_2O_3-based anodes is still low and cannot match that of cathodes in the full cells. In this work, a composite material with well dispersed Fe_2O_3 quantum dots (QDs, ≈2 nm) decorated on functionalized graphene-sheets (FGS) is prepared by a facile and scalable method. The Fe_2O_3 QDs/FGS composites exhibit a large specific capacitance up to 347 F g^{-1} in 1 M Na_2SO_4 between −1 and 0 V versus Ag/AgCl. An asymmetric supercapacitor operating at 2 V is fabricated using Fe_2O_3/FGS as anode and MnO_2/FGS as cathode in 1 M Na_2SO_4 aqueous electrolyte. The Fe_2O_3/FGS//MnO_2/FGS asymmetric supercapacitor shows a high energy density of 50.7 Wh kg^{-1} at a power density of 100 W kg^{-1} as well as excellent cycling stability and power capability. The facile synthesis method and superior supercapacitive performance of the Fe_2O_3 QDs/FGS composites make them promising as anode materials for high-performance asymmetric supercapacitors.

1. Introduction

Supercapacitors, also called as electrochemical capacitors, have attracted considerable attention as energy storage devices for various applications such as portable electronics and electric vehicles, which can be attributed to their desirable characteristics of high power density, fast rates of charge and discharge, excellent cycling stability, and low maintenance cost.[1–5] However, for practical

applications in various electronic devices, the energy density of current supercapacitors need to be further improved without sacrificing the power density and cycle life. According to the equation of energy density $E = 1/2CV^2$, the specific energy of supercapacitors can be increased by increasing the output voltage (V) and/or the specific capacitance.[6] An effective way to increase the operation voltage is to use ionic liquids or organic electrolytes, which, however, suffer from the poor ionic conductivity, short cycle life, and toxicity, making them undesirable in practical applications.[7] A more desirable strategy is to construct asymmetric supercapacitors using environmentally friendly aqueous electrolytes with fast ion transport. For asymmetric supercapacitors, different negative and positive electrode materials having well-separated potential windows are coupled to maximize the output voltage.[8]

MnO_2-based materials, exhibiting large specific capacitance and high overpotential for oxygen evolution, are usually employed as cathode materials for asymmetric supercapacitors using neutral aqueous electrolytes.[9,10] Carbon-based materials, especially activated carbon (AC), are usually used as anode materials due to their large surface, excellent electrical conductivity, and good power capability.[11] However, the low specific capacitance of carbon materials cannot match the high specific capacitance of MnO_2-based materials, thus

Prof. H. Xia, C. Hong, B. Li
School of Materials Science and Engineering
Nanjing University of Science and Technology
Xiaolingwei 200, Nanjing 210094, China
E-mail: xiahui@njust.edu.cn
Prof. H. Xia, C. Hong, B. Li
Herbert Gleiter Institute of Nanoscience
Nanjing University of Science and Technology
Xiaolingwei 200, Nanjing 210094, China
B. Zhao, Z. Lin, Prof. M. Zheng
Nanjing National Laboratory of Microstructures
School of Electronic Science and Engineering
Nanjing University
Nanjing 210093, China
E-mail: zhengmingbo@nju.edu.cn

Prof. S. V. Savilov
Department of Chemistry
M. V. Lomonosov Moscow State University
Moscow 119991, Russia
Prof. S. M. Aldoshin
Department of Physical Chemistry Engineering
M. V. Lomonosov Moscow State University
Moscow 119991, Russia

FULL PAPER

limiting the energy density for asymmetric supercapacitors.[12] Great efforts have been devoted to studying transition metal oxides, such as MoO_{3-x}, V_2O_5, VN, RuO_2, Bi_2O_3, and FeO_x, to achieve large specific capacitance for the anode materials.[13–19] Among them, Fe_2O_3 attracts considerable attention because of its large overpotential for hydrogen evolution, low cost, and natural abundance.[20] Recently, several works have reported the successful application of Fe_2O_3 as anode for asymmetric supercapacitors.[21,22] However,

Scheme 1. Schematic illustration of the composite electrode design and the construction of asymmetric supercapacitor.

small surface area and poor electronic conductivity are still two obstacles that limit the specific capacitance and power capability of Fe_2O_3. In order to circumvent these problems, graphite carbons such as carbon nanotubes and carbon nanofibers are harnessed as conductive matrices to load Fe_2O_3 nanoparticles for improved performance.[23,24] Particularly, graphene, possessing large surface area and excellent electronic conductivity, has become one of the most appealing matrices for Fe_2O_3.[25–27] It is noteworthy, on the other hand, that the size and dispersion of Fe_2O_3 particles on graphene are crucial factors determining the electrode performance. Small particle size plus good dispersion can endow the composite electrode a superior high surface area and required conductivity,[28,29] which are beneficial for large specific capacitance and good power capability. According to literature, however, most Fe_2O_3/graphene composites prepared so far have relatively large particle size (>10 nm) for Fe_2O_3 with unsatisfying dispersions. Apart from that, the main routes commonly used for the preparation of the Fe_2O_3/graphene composites were carried out with complicated processes, which are not applicable for large scale production.

In this work, we designed a facile, scalable, and one-step thermal decomposition method to synthesize Fe_2O_3 quantum dots (QDs) ($\approx$2 nm) decorated on functionalized graphene-sheets (FGS) at a low temperature of 200 °C. For the composite, FGS with oxygen functional groups on the surface were used as the conductive matrix and the surface defective sites serve as the initial nucleation sites for the controllable growth of Fe_2O_3 QDs.[30] With a proper control for the Fe_2O_3/FGS mass ratio, Fe_2O_3 QDs can be well dispersed on the FGS without aggregation and a large specific capacitance of about 347 F g^{-1} can be obtained. To the best of our knowledge, this specific capacitance is the highest value has ever been reported for the Fe_2O_3-based electrode materials using neutral aqueous electrolytes for supercapacitors. Moreover, a 2 V asymmetric supercapacitor was then successfully constructed by coupling a Fe_2O_3/FGS anode and a MnO_2/FGS cathode. As expected, the Fe_2O_3/FGS//MnO_2/FGS asymmetric supercapacitor exhibited large energy density as well as outstanding cycling stability and power capability.

2. Results and Discussion

Scheme 1 illustrates the composite electrode design and construction of the asymmetric supercapacitor. A simple thermal decomposition method was designed to prepare Fe_2O_3/FGS composite as the anode material. It simply involves the mixing of
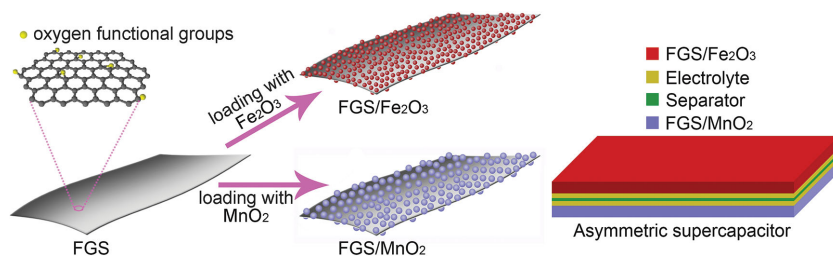
FGS and iron salt in solution and thermal annealing of the mixture in air. The existence of covalent chemical bonding formed through oxygen-containing defect sites on the graphene surface (Supporting Information Figure S1) provides an opportunity to tightly achor iron oxide on graphene. This method is scalable and applicable to other metal oxide/graphene composites. In the present study, MnO_2/FGS composite was prepared as the cathode material using the similar method.

Figure 1a shows the X-ray diffraction (XRD) patterns of the pristine FGS, Fe_2O_3, and Fe_2O_3/FGS composites with different
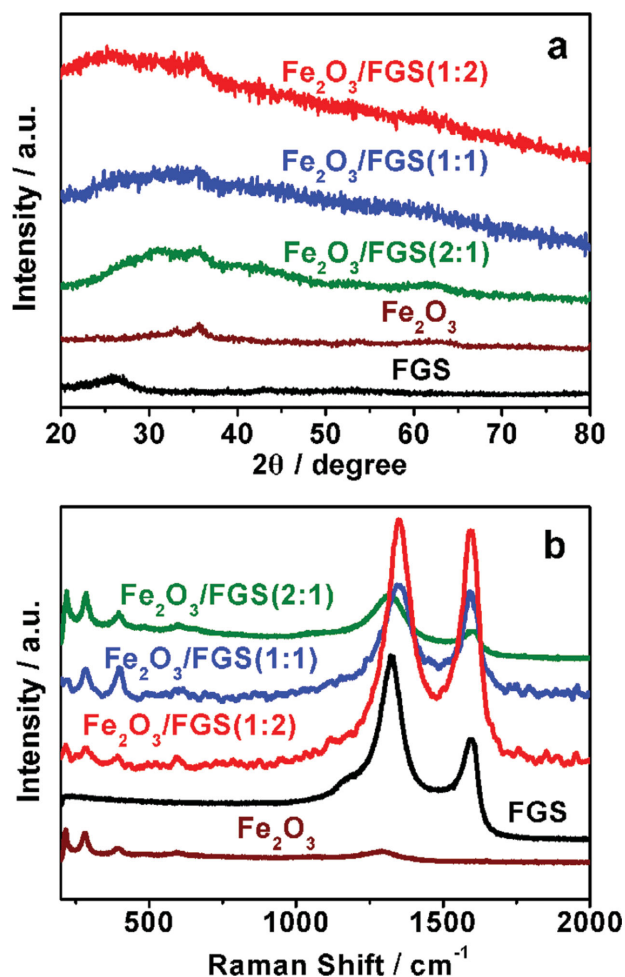
Figure 1. XRD patterns a) and the Raman spectra b) of the pristine FGS, pure Fe_2O_3, and Fe_2O_3/FGS composites with different Fe_2O_3/FGS mass ratios.

www.MaterialsViews.com

ADVANCED
FUNCTIONAL
MATERIALS
www.afm-journal.de

FULL PAPER
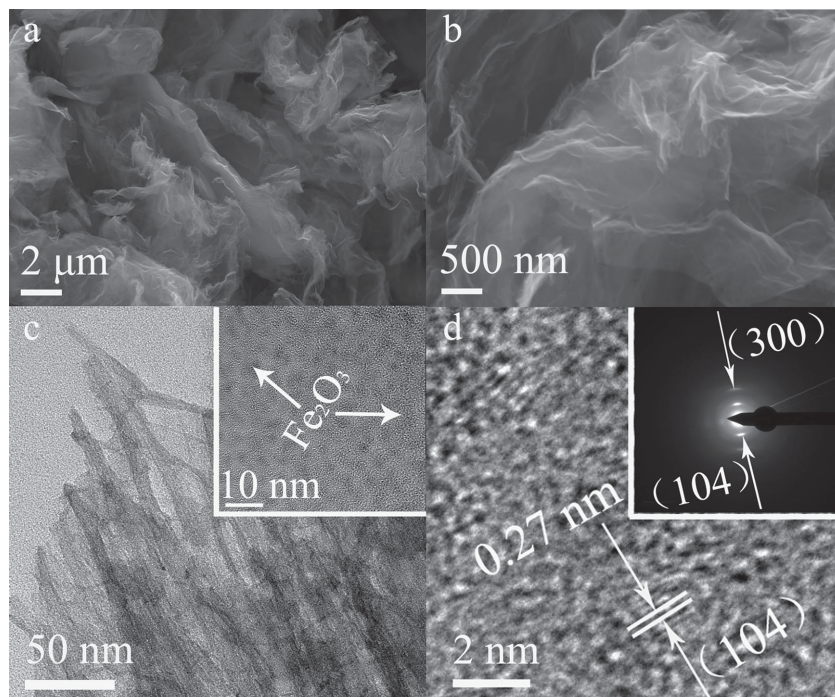
Figure 2. a,b) FESEM images of the Fe_2O_3/FGS composite (1:1 sample). c) TEM and d) HRTEM images of the Fe_2O_3/FGS composite (1:1 sample). The inset in c) shows a HRTEM image of the Fe_2O_3/FGS composite. The inset in d) shows the SAED pattern of the Fe_2O_3/FGS composite.

Fe_2O_3/FGS mass ratios (1:2, 1:1, 2:1). The pristine Fe_2O_3 XRD pattern shows two small diffraction peaks located at 34° and 35°, which can be attributed to the (104) and (110) reflections of α-Fe_2O_3 (JCPDS no. 33–0664). Small humps at similar locations were also observed for the XRD patterns of the Fe_2O_3/FGS composites, indicating nanocrystalline feature and/or low degree of crystallinity of the Fe_2O_3 particles. The pristine FGS XRD pattern shows a small hump at about 26°, which can be attributed to the (002) reflection of graphite. Such small hump is also observed in the XRD patterns of the Fe_2O_3/FGS composites, probably indicating graphene sheets are highly disordered stacking with low degree of graphitization.[27] Figure 1b shows the Raman spectra of the pristine FGS, Fe_2O_3, and Fe_2O_3/FGS composites with different Fe_2O_3/FGS mass ratios. The D-band located at 1325 cm^{-1} and the G-band at 1598 cm^{-1} are characteristic Raman shifts of graphite, which can be observed in the Raman spectra of both FGS and Fe_2O_3/FGS composites. Four Raman shifts can be observed between 200 and 700 cm^{-1} for the pristine Fe_2O_3 and Fe_2O_3/FGS composites, which correspond to one A_{1g} (218 cm^{-1}) and three E_g (284, 397, and 594 cm^{-1}) Raman modes of α-Fe_2O_3.[31] The XRD and Raman results confirm the successful synthesis of Fe_2O_3/FGS composite without trace of impurity phase.

The morphology and microstructure of the Fe_2O_3/FGS composite (1:1) was investigated by field emission scanning electron microscopy (FESEM) and transmission electron microscopy (TEM). **Figure 2**a and 2b show the FESEM images of the Fe_2O_3/FGS composite with low and high magnifications, respectively, revealing a 2D morphology comprising of crumpled nanosheets with numerous wrinkles and folds. Numerous macropores are

observed between the nanosheets, which results from the thermal exfoliation of FGS. It is not able to observe the Fe_2O_3 particles on FGS by FESEM due to the small particle size. Figure 2c shows the TEM image of the Fe_2O_3/FGS composite (1:1), revealing uniform dispersion of Fe_2O_3 nanoparticles on the transparent FGS without severe aggregation. The enlarged TEM image inserted in Figure 2c shows that the mean particle size for the Fe_2O_3 QDs is about 2 nm. The bare Fe_2O_3 QDs synthesized by the similar thermal decomposition method show similar particle size (Supporting Information Figure S2). The pores between the Fe_2O_3 QDs have the similar size as the particles, representing a mesoporous structure for the Fe_2O_3 layer coated on the FGS. The high-resolution transmission electron microscopy (HRTEM) image of the Fe_2O_3 QDs in Figure 2d shows clear lattice fringes with a interplanar spacing of 0.27 nm, which can be attributed to the (104) plane of Fe_2O_3. The selected area electron diffraction (SAED) pattern (inset in Figure 2d) shows two diffraction rings, corresponding to the (104) and (300) planes of Fe_2O_3, respectively. The carbon contents determined from the thermogravimetric analysis (TGA) for the three Fe_2O_3/FGS composites (Supporting Information Figure S3) are 72, 53, and 34 wt%, respectively. In convenience, 1:2, 1:1, and 2:1 are still used in the following text to denote different Fe_2O_3/FGS composites.

The nitrogen adsorption–desorption isotherms and the pore size distributions of the Fe_2O_3/FGS composites with different Fe_2O_3/FGS mass ratios are shown in **Figure 3**. Similar to FGS (Supporting Information Figure S4), all Fe_2O_3/FGS composites show typical type-IV isotherms (Figure 3a), indicating the existence of mesopores in the composites. The pore size distributions of the samples calculated by adsorption isotherm using Barret–Joyner–Halenda (BJH) method are shown in Figure 3b. Agreeing with the TEM results, all Fe_2O_3/FGS composites show a pore size distribution below 5 nm, which could be mainly contributed by the space between the Fe_2O_3 QDs. For comparison, Brunauer–Emmett–Teller specific surface areas and pore volumes of the pristine FGS and Fe_2O_3/FGS composites are summarized in Table S1 (Supporting Information). The specific surface areas are 216.5, 208.0, and 198.5 m^2 g^{-1} for the 1:2, 1:1, and 2:1 Fe_2O_3/FGS composites, respectively, as a result of the overall reduction in the specific surface area with increased mass loading of Fe_2O_3. The large surface area of the Fe_2O_3/FGS composites undoubtedly shortens the ion diffusion paths and improves the utilization of active materials, which may lead to improved pseudocapacitive performance for the composite electrodes.
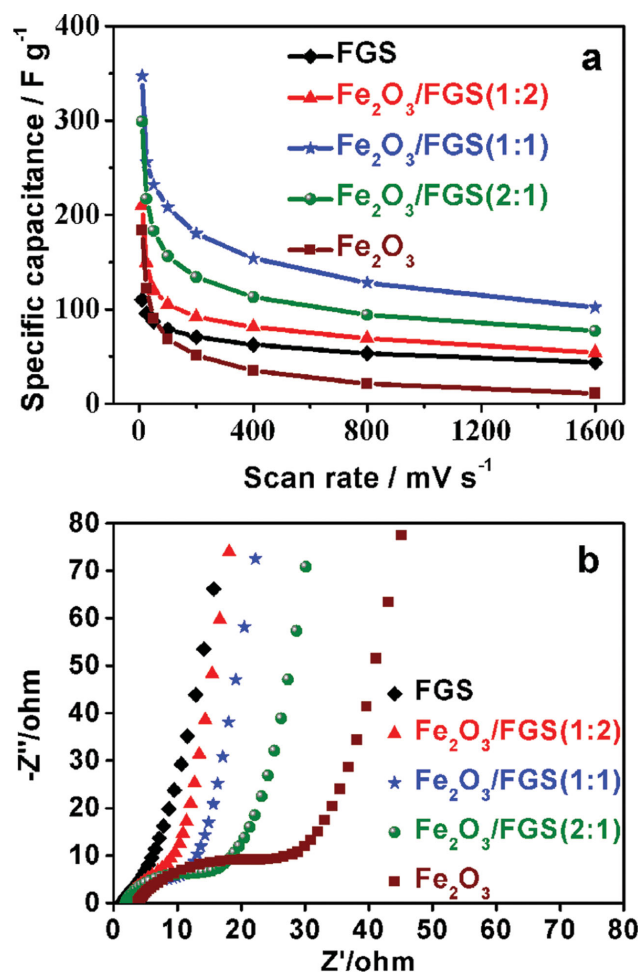
The large surface area and good electrical conductivity will endow the composite electrodes with promising electrochemical performance for supercapacitors. Three Fe_2O_3/FGS composites with different Fe_2O_3/FGS mass ratios were
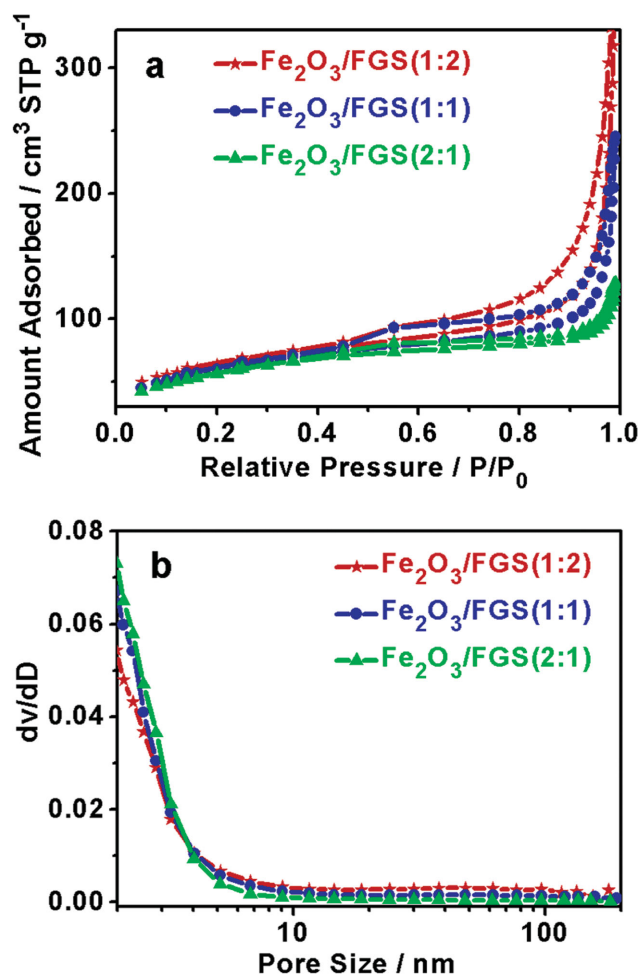
Figure 3. N$_2$ adsorption–desorption isotherms a) and BJH pore size distribution plots b) of the Fe$_2$O$_3$/FGS composites with different Fe$_2$O$_3$/FGS mass ratios at 77 K.

Figure 4. a) Specific capacitances of the pristine FGS, Fe$_2$O$_3$, and Fe$_2$O$_3$/FGS composite electrodes as a function of CV scan rate. b) Nyquist plots of the pristine FGS, Fe$_2$O$_3$, and Fe$_2$O$_3$/FGS composite electrodes.

investigated by cyclic voltammogram (CV), and their CV curves were compared with those of the pristine FGS and Fe$_2$O$_3$ (Supporting Information Figure S5). The CV measurements were carried out in three-electrode cells between –1 and 0 V versus Ag/AgCl in 1 M Na$_2$SO$_4$ electrolyte at different scan rates from 10 to 1600 mV s^{-1}. For all scan rates, the CV curves of the pristine FGS electrode remain the rectangular shape without distortion, indicating ideal capacitive behavior. On the contrary, the CV curves of the pristine Fe$_2$O$_3$ electrode are seriously distorted, especially at high scan rates, indicating large cell polarization due to the high resistance of the Fe$_2$O$_3$ electrode. Remarkably, it is noted that the CV curves of the Fe$_2$O$_3$/FGS composite electrodes can still maintain good rectangularity even at high scan rates such as 1600 mV s^{-1}, similar to the behavior of the FGS electrode. Only for the 2:1 sample, the CV curves are slightly distorted from the rectangular shape at high scan rates, which is probably due to the large content of Fe$_2$O$_3$ in the composite. The specific capacitances of the pristine FGS, Fe$_2$O$_3$, and Fe$_2$O$_3$/FGS composite electrodes as a function of scan rate are compared in **Figure 4**a. Although the FGS electrode exhibits outstanding CV behavior, its specific capacitance is only about 120 F g^{-1} at the scan rate of 10 mV s^{-1}. At the

same scan rate, the Fe$_2$O$_3$ electrode exhibits a relatively larger specific capacitance of about 200 F g^{-1}, whereas it decreases quickly as the scan rate increases, indicating poor rate capability. When FGS is incorporated into Fe$_2$O$_3$ QDs, the Fe$_2$O$_3$/FGS composite electrodes display significantly enhanced specific capacitance as well as superior rate performance. In specific, the 1:1 Fe$_2$O$_3$/FGS composite electrode exhibits a specific capacitance up to 347 F g^{-1} at a scan rate of 10 mV s^{-1}, which is the largest value reported for the Fe$_2$O$_3$-based electrodes in neutral aqueous electrolytes. **Table 1** summarizes the reported electrochemical performance of the Fe$_2$O$_3$-based electrodes in neutral aqueous electrolytes.[32–37] Compared with the previously reported Fe$_2$O$_3$-based electrodes, the Fe$_2$O$_3$ QD/FGS composite electrodes developed in the present work possess obvious advantages in terms of specific capacitance and rate capability, which could be attributed to the synergetic effect of high conductivity of FGS and large capacitance contribution from Fe$_2$O$_3$ QDs. It is also noted that the mass ratio of Fe$_2$O$_3$/FGS is crucial to the electrochemical performance of the composite electrodes. In specific, the 1:1 Fe$_2$O$_3$/FGS composite electrode shows larger specific capacitance compared with the 1:2 and 2:1 composite electrodes. To understand the difference

Table 1. Comparison of electrochemical performance for the Fe_2O_3-based electrodes in negative potential windows in neutral aqueous electrolytes.
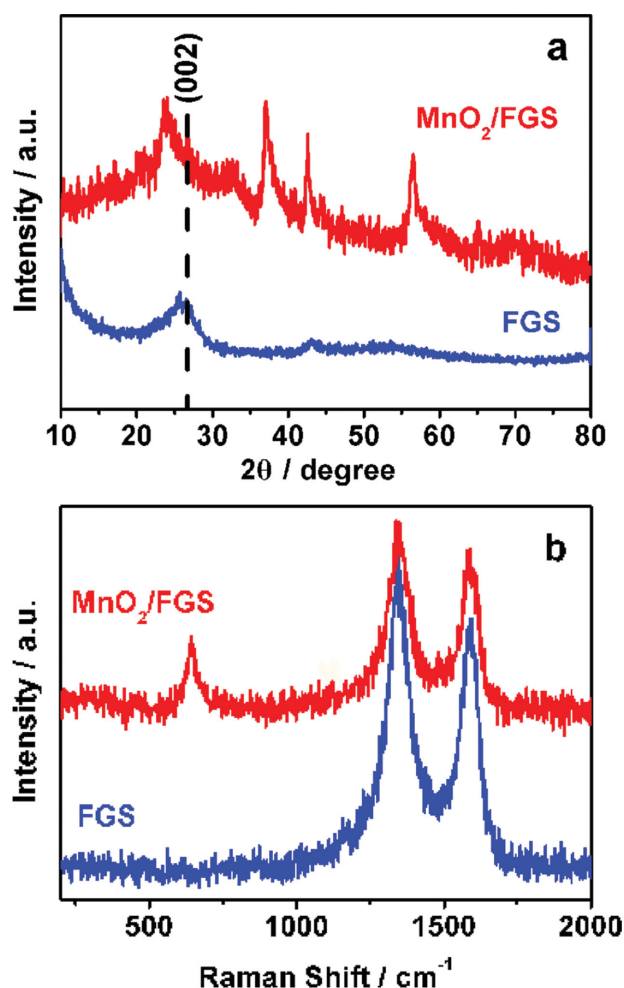
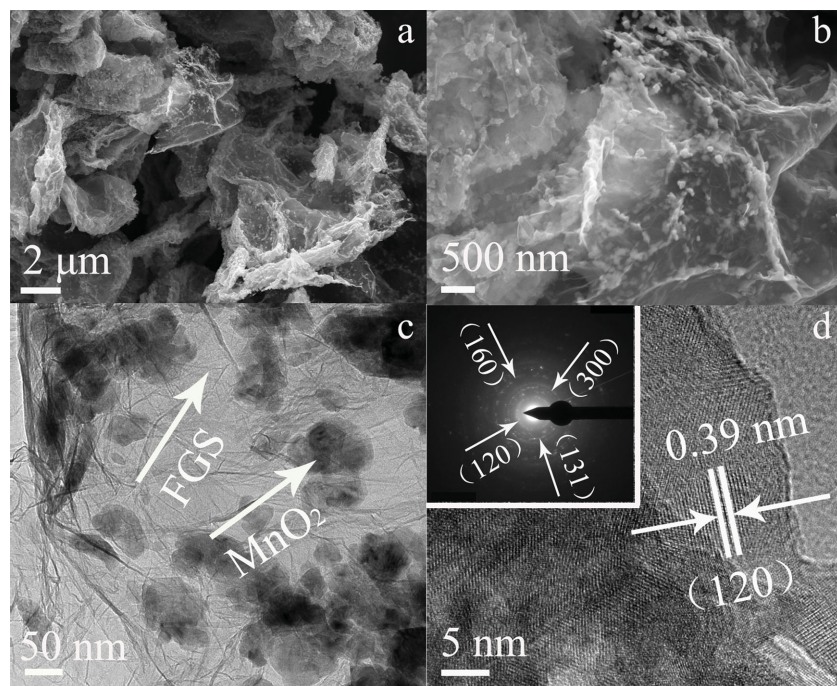| Fe_2O_3-based electrode	Electrolyte	Potential range [V vs. Ag/AgCl or SCE]	Specific capacitance [F g^{-1}]	Rate capability [F g^{-1}]	Ref. (year)
Fe_2O_3 nanosheet film	1 M Li_2SO_4	−0.9 to −0.1 V	173 at 3 A g^{-1}	117 at 12.3 A g^{-1}	(2009) [29]
Fe_2O_3 nanotube arrays	1 M Li_2SO_4	−0.6 to 0 V	138 at 1.3 A g^{-1}	91 at 12.8 A g^{-1}	(2011) [30]
Fe_2O_3 nanotube/rGO	1 M Na_2SO_4	−1 to 0 V	215 at 2.5 mV s^{-1}	88 at 100 mV s^{-1}	(2012) [22]
Fe_2O_3 sheets on nickel foam	1 M Li_2SO_4	−0.8 to −0.2 V	147 at 0.36 A g^{-1}	98 at 3.6 A g^{-1}	(2014) [31]
Fe_2O_3 mesocrystals/graphene	1 M Na_2SO_4	−1.2 to −0.2 V	306 at 3 A g^{-1}	98 at 10 A g^{-1}	(2014) [24]
Fe_2O_3/graphene composite	1 M Na_2SO_4	−1.2 to −0.2 V	193 at 5 mV s^{-1}	100 at 100 mV s^{-1}	(2014) [32]
Fe_2O_3/mesoporous carbon	1 M Na_2SO_3	−1.0 to −0.2 V	235 at 0.5 A g^{-1}	119 at 10 A g^{-1}	(2014) [33]
Flower-like Fe_2O_3 nanostructures	0.5 M Na_2SO_3	−0.8 to 0 V	127 at 1 A g^{-1}	40 at 14 A g^{-1}	(2013) [34]
Fe_2O_3 QDs/FGS	1 M Na_2SO_4	−1 to 0 V	347 at 10 mV s^{-1}	140 at 1600 mV s^{-1}	This work

in capacitive performance for the Fe_2O_3/FGS composite electrodes, electrochemical impedance spectroscopy (EIS) measurements were carried out and the obtained Nyquist plots, are shown in Figure 4b. The 1:2 Fe_2O_3/FGS composite electrode shows only slightly larger charge transfer resistance compared with the pristine FGS electrode, indicating excellent electrical conductivity for this composite electrode. The charge transfer resistance increases as the Fe_2O_3 content increases in the composite, indicating that having a high Fe_2O_3 content in the composite will take the price of low electrical conductivity. Apart from the large charge transfer resistance, the 2:1 Fe_2O_3/FGS composite also has a lower specific surface area, resulting in a low utilization of Fe_2O_3 and smaller specific capacitance compared with the 1:1 sample. On the other hand, if the Fe_2O_3 content is too low in the composite (such as the 1:2 sample), the specific capacitance could be mainly contributed by the FGS, which will also lead to a decrease in the specific capacitance. Therefore, the Fe_2O_3/FGS mass ratio in the composite is a crucial factor to achieve the best electrochemical performance. In the present work, the 1:1 Fe_2O_3/FGS composite represent the best electrode design as anode for asymmetric supercapacitors.

To build the asymmetric supercapacitors, MnO_2/FGS composite with 37 wt% FGS (Supporting Information Figure S2) was synthesized as cathode material by the similar thermal decomposition method. **Figure 5**a shows the XRD patterns of the pristine FGS and the MnO_2/FGS composite. Except for the (002) reflection from FGS, all other diffraction peaks can be indexed to γ-MnO_2 (JCPDS No. 14–0644).[38] Figure 5b shows the Raman spectra of the pristine FGS and MnO_2/FGS composite. Together with D and G bands for FGS, the Raman spectrum of the MnO_2/FGS composite also shows a Raman band located at about 650 cm^{-1}, which can be attributed to the Mn–O vibration perpendicular to the direction of the MnO_6 octahedral double chains of MnO_2.[39] The XRD and Raman results confirm the successful preparation of the MnO_2/FGS composite by the thermal decomposition method.

The morphology for the MnO_2/FGS composite was investigated by FESEM and TEM. **Figure 6**a,b shows the FESEM images for the MnO_2/FGS composite with low and high magnifications, respectively. It can be seen that MnO_2 nanoparticles are uniformly dispersed on the crumpled FGS without severe aggregation, revealing a similar porous structure as the Fe_2O_3/

FGS composite. Figure 6c shows the TEM image for the MnO_2/FGS composite, showing that the particle size of MnO_2 is in the range of 50–100 nm. The HRTEM image in Figure 6d shows clear lattice fringes for the MnO_2 nanoparticles, indicating a high degree of crystallinity. The crystal lattice with a spacing of 0.40 nm corresponds to the (110) plane of γ-MnO_2. In

Figure 5. a) XRD patterns and b) Raman spectra of the pristine FGS and MnO_2/FGS composite.

**ADVANCED
FUNCTIONAL
MATERIALS**

www.afm-journal.de

*Materials
Views*

www.MaterialsViews.com

Figure 6. a,b) FESEM images of the MnO$_2$/FGS composite. c) TEM and d) HRTEM images of the MnO$_2$/FGS composite. The inset in (d) shows the SAED pattern for the MnO$_2$/FGS composite.

addition, the SAED pattern (inset in Figure 6d) shows a set of diffraction rings, which can be clearly assigned to the diffractions of the (111), (220), and (222) planes, respectively, confirming the formation of γ-MnO$_2$ on FGS.

Figure 7a,b shows the CV curves of the Fe$_2$O$_3$/FGS (1:1) composite electrode and the MnO$_2$/FGS composite electrode in negative (–1 to 0 V vs Ag/AgCl) and positive (0 to 1 V vs Ag/AgCl) potential windows, respectively, at different scan rates. Similar to the Fe$_2$O$_3$/FGS composite electrode, the MnO$_2$/FGS composite electrode exhibits rectangular shaped CV curves at various scan rates with near mirror-image current response on voltage reversal, indicating ideal capacitive behavior for the MnO$_2$/FGS composite electrode in the positive potential window. Figure 7c compares the specific capacitances of the Fe$_2$O$_3$/FGS composite electrode and the MnO$_2$/FGS composite electrode at different scan rate from 10 to 1600 mV s^{-1}. It can be seen that the specific capacitances of the MnO$_2$/FGS composite electrode are in good match with those of the Fe$_2$O$_3$/FGS composite electrode at various scan rates, indicating the negative electrode and
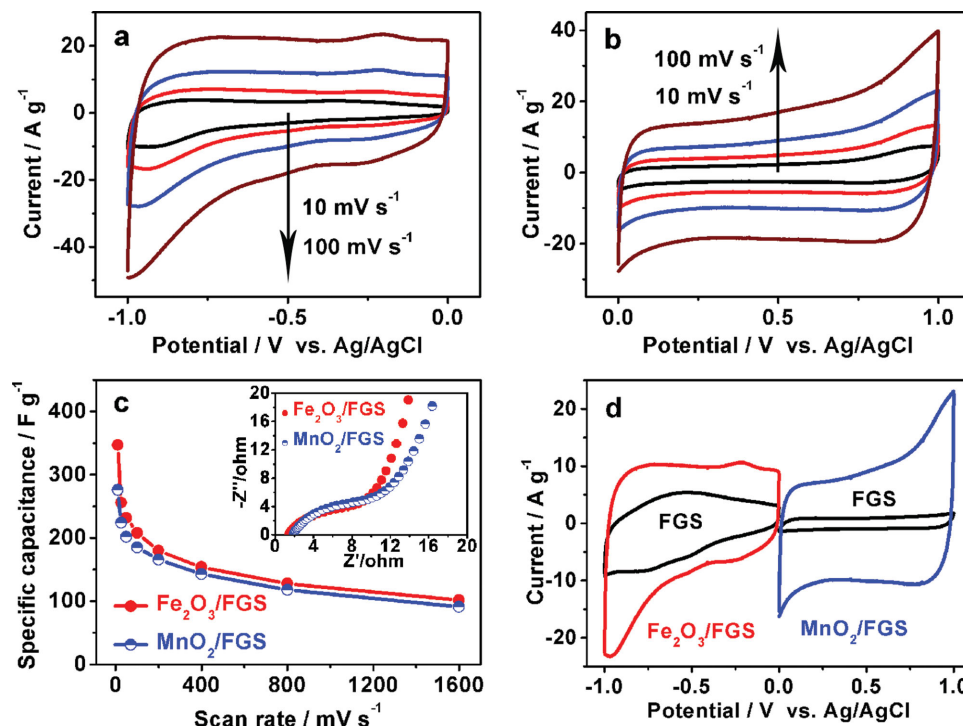
Figure 7. The CV curves of the Fe$_2$O$_3$/FGS (1:1) composite electrode a) in negative voltage window (–1 to 0 V vs Ag/AgCl) and the MnO$_2$/FGS composite electrode b) in positive voltage window (0 to 1 V vs Ag/AgCl) at different scan rates. c) The specific capacitances of the Fe$_2$O$_3$/FGS (1:1) composite electrode and the MnO$_2$/FGS composite electrode as a function of CV scan rate. Inset in c) shows the EIS spectra of the MnO$_2$/FGS and Fe$_2$O$_3$/FGS composite electrodes. d) The comparison of CV curves of the Fe$_2$O$_3$/FGS (1:1) composite, the MnO$_2$/FGS composite and the pristine FGS electrodes in –1 to 0 and 0 to 1 V potential windows at a scan rate of 50 mV s^{-1}.

www.MaterialsViews.com

ADVANCED
FUNCTIONAL
MATERIALS
www.afm-journal.de

FULL PAPER
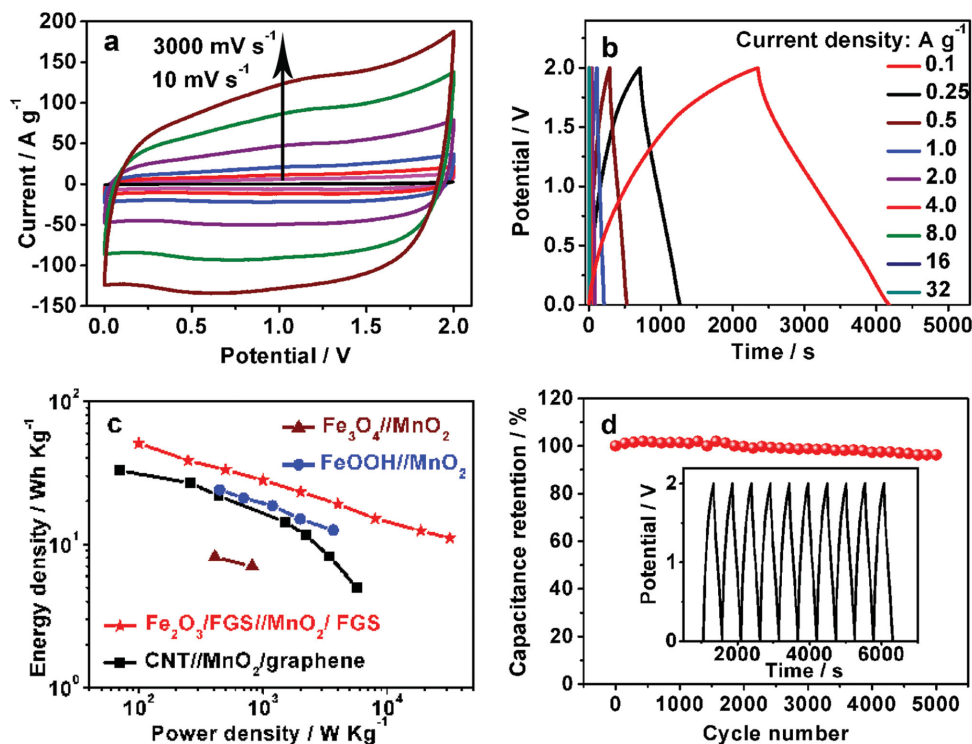
Figure 8. a) The CV curves of the $Fe_2O_3/FGS//MnO_2/FGS$ asymmetric supercapacitor between 0 and 2 V at different scan rates from 10 to 3000 mV s^{-1}. b) The galvanostatic charge/discharge curves of the asymmetric supercapacitor at different current densities. c) The Ragone plots of the $Fe_2O_3/FGS//MnO_2/FGS$ asymmetric supercapacitor compared with reported data in literature. d) The cycle performance of the $Fe_2O_3/FGS//MnO_2/FGS$ asymmetric supercapacitor.

positive electrode can be ideally coupled to make the asymmetrical supercapacitor. Inset in Figure 7c shows the Nyquist plots for both the Fe_2O_3/FGS composite electrode and the MnO_2/FGS composite electrode. The MnO_2/FGS composite electrode exhibits a similar small charge transfer resistance as the Fe_2O_3/FGS composite electrode, indicating the hybrid electrode design is efficient to achieve fast electrode kinetics. Based on the operating voltage window determined by the CV results (Figure 7d), an asymmetric supercapacitor using the Fe_2O_3/FGS anode and the MnO_2/FGS cathode is expected to have a high working voltage up to 2 V in 1 M Na_2SO_4. As shown in Figure 7d, the pristine FGS electrode also shows good electrochemical stability in both negative and positive voltage windows, indicating the possibility to build a 2 V symmetric supercapacitor by using two FGS electrodes (also see Supporting Information Figure S6). However, the CV curves of the pristine FGS electrode show much smaller loop areas compared with those of the Fe_2O_3/FGS the MnO_2/FGS composited electrodes, indicating much lower specific capacitance and lower energy density for building the symmetric supercapacitor. An asymmetric supercapacitor was fabricated by using the Fe_2O_3/FGS as anode and the MnO_2/FGS as cathode in a two-electrode Swagelok cell. **Figure 8**a shows the CV curves of the $Fe_2O_3/FGS//MnO_2/FGS$ asymmetric supercapacitor between 0 and 2 V at different scan rates from 10 to 3000 mV s^{-1} in 1 M Na_2SO_4 aqueous solution. Noticeably, the CV curves retain good rectangularity even at a high scan rate of 3000 mV s^{-1}, indicating small resistance of the full cell and excellent rate

capability. Based on the total mass of active materials from both anode and cathode, the specific capacitance of the asymmetric supercapacitor was calculated to be about 73.2 F g^{-1} at a scan rate of 10 mV s^{-1}. Even at a high scan rate of 3000 mV s^{-1}, the full cell can still deliver a specific capacitance of about 36.3 F g^{-1}. A 2 V FGS//FGS symmetric supercapcitor has been successfully constructed for comparison and its CV curves at different scan rates exhibit ideal rectangular shape (Supporting Information Figure S7). However, the specific capacitance for the FGS//FGS symmetric supercapacitor is only about 32.2 F g^{-1} at a scan rate of 10 mV s^{-1}, which is much lower than that of the $Fe_2O_3/FGS//MnO_2/$ FGS asymmetric supercapacitor. The large specific capacitance and excellent rate capability of the $Fe_2O_3/FGS//MnO_2/FGS$ asymmetric supercapacitor could be attributed to the composite electrode design for both anode and cathode with large surface area and good electrical conductivity. Galvanostatic charge/discharge measurements were further carried out on the asymmetric supercapacitor between 0 and 2 V at various current densities from 0.1 to 32 A g^{-1}. As shown in Figure 8b, the charge/discharge curves at various current densities show the typical triangular shape with linear voltage time relation, indicating ideal capacitive behavior. Based on the charge/discharge curves, the energy densities and power densities for the $Fe_2O_3/FGS//MnO_2/FGS$ asymmetric supercapacitor at various current densities are shown in the Ragone plots (Figure 8c) to compare with those of other reported symmetric/asymmetric supercapacitors. Remarkably, the present $Fe_2O_3/FGS//MnO_2/FGS$ asymmetric supercapacitor can deliver

ADVANCED
FUNCTIONAL
MATERIALS
www.afm-journal.de

Materials Views
www.MaterialsViews.com

a maximum energy density of about 50.7 Wh kg^{-1} at a power density of 100 W kg^{-1}, which is significantly larger than those of symmetric supercapacitors, such as MnO$_2$/graphene//MnO$_2$/graphene supercapacitors (8.1 Wh kg^{-1}),[40] AC//AC supercapacitors (<10 Wh kg^{-1}),[41] and MnO$_2$//MnO$_2$ supercapacitors (<3.3 Wh kg^{-1}),[42] and also larger than those of asymmetric supercapacitors of CNT//MnO$_2$/graphene (32.7 Wh kg^{-1}),[43] AC//MnO$_2$ (28.8 Wh kg^{-1}),[44] FeOOH//MnO$_2$(12 Wh kg^{-1}),[45] and Fe$_3$O$_4$//MnO$_2$ (8.1 Wh kg^{-1}). [42] Even at a high power density of 32 kW kg^{-1}, the Fe$_2$O$_3$/FGS//MnO$_2$/FGS asymmetric supercapacitor still can reach an energy density of about 10 Wh kg^{-1}, indicating superior power capability. Apart from the outstanding power capability, the Fe$_2$O$_3$/FGS//MnO$_2$/FGS asymmetric supercapacitor also exhibits excellent cycle performance. Figure 8d shows the capacitance retention of the Fe$_2$O$_3$/FGS//MnO$_2$/FGS asymmetric supercapacitor as a function of cycle number at a current density of 0.5 A g^{-1} for 5000 charge/discharge cycles. About 95% of its initial capacitance was retained after 5000 cycles, indicating good cycling stability for the asymmetric system. Such good cycle performance is comparable with that of other asymmetric supercapacitors and is highly promising for practical applications.

Compared with previously reported asymmetric supercapacitors, the present Fe$_2$O$_3$/FGS//MnO$_2$/FGS asymmetric supercapacitor exhibits superior energy and power densities, which can be attributed to the unique composite electrode design and rational cathode–anode coupling. The carbon-based anodes usually limit the energy density of the asymmetric supercapacitors due to their relative lower specific capacitance. The present Fe$_2$O$_3$ QDs/FGS composite exhibits greatly improved specific capacitance due to the synergetic effect of highly conductive FGS providing fast electron transfer and large surface area and well-dispersed Fe$_2$O$_3$ QDs contributing large pseudocapacitance. The thermal decomposition is a facile yet efficient method to synthesize high-quality Fe$_2$O$_3$ QDs/FGS composite for application in asymmetric supercapacitors. In the composite electrode, FGS not only provides fast electron transfer in the electrode but also suppresses the agglomeration of Fe$_2$O$_3$ QDs. The size down to several nanometers, good dispersivity of Fe$_2$O$_3$ QDs, and the compact contact between Fe$_2$O$_3$ QDs and FGS are beneficial for maximizing the specific capacitance for the composite electrode. The large specific capacitance of the present Fe$_2$O$_3$ QDs/FGS composite is comparable with that of the MnO$_2$/FGS composite, making the desirable anode–cathode coupling to build a 2 V asymmetric supercapacitor with both high energy density and power density.

3. Conclusion

In summary, we have presented a facile method to synthesize Fe$_2$O$_3$ QDs/FGS composites featuring several nanometer sized Fe$_2$O$_3$ QDs well dispersed on FGS with large surface area. The Fe$_2$O$_3$/FGS mass ratio in the composites plays an important role in determining the supercapacitive performance of the composite electrodes. As the FGS content was tuned to 53 wt%, the Fe$_2$O$_3$/FGS composite electrode can reach a maximum specific capacitance of about 347 F g^{-1}, which is much larger than the reported values for the Fe$_2$O$_3$-

based electrodes in neutral aqueous electrolyte. Besides large specific capacitance, the Fe$_2$O$_3$/FGS composite electrode also exhibits excellent rate capability, which can be attributed to the synergetic effect of the highly conductive FGS and ultrafine Fe$_2$O$_3$ QDs. A 2 V asymmetrical supercapacitor has been fabricated using Fe$_2$O$_3$/FGS as anode and MnO$_2$/FGS as cathode in 1 M Na$_2$SO$_4$ electrolyte. The Fe$_2$O$_3$/FGS//MnO$_2$/FGS asymmetric supercapacitor can deliver an energy density of 50.7 Wh kg^{-1} at a power density of 100 W kg^{-1} and an energy density of 10 Wh kg^{-1} at a power density of 32 kW kg^{-1}, indicating outstanding energy density and power density. In addition to high energy density and power density, the asymmetric supercapacitor also exhibits good cycling stability with 95% of initial capacitance retained after 5000 cycles. The facile electrode material synthesis and superior supercapacitive performance make the Fe$_2$O$_3$/FGS//MnO$_2$/FGS asymmetric supercapacitors promising for practical applications in high performance energy storage systems.

4. Experimental Section

Synthesis of FGS: Graphene oxide (GO) was synthesized from purified natural graphite according to the method reported by Hummers and Offeman.[46] The dried GO was thermally exfoliated at 300 °C for 5 min under air atmosphere, and then treated at 900 °C in N$_2$ for 3 h with a heating rate of 2 °C min^{-1} to obtain the functionalized FGS.[47]

Synthesis of Fe$_2$O$_3$ QDs/FGS Composites and MnO$_2$/FGS Composites: The Fe$_2$O$_3$ QDs/FGS composites were synthesized by a facile thermal decomposition method. In a typical synthesis, certain amount of Fe(NO$_3$)$_3$·9H$_2$O was first dissolved in ethanol (35 mL). 50 mg FGS was then added into the solution followed by 10 min ultrasonication to form a suspension. The suspension was magnetically stirred in a fume hood with slow evaporation of ethanol. After evaporation, the sample was collected and dried at 40 °C for 24 h in a blast drying oven. The dried Fe(NO$_3$)$_3$·9H$_2$O/FGS composite was finally heated at 200 °C in an oven for 10 h to obtain the Fe$_2$O$_3$ QDs/FGS composite. Various amounts of Fe(NO$_3$)$_3$·9H$_2$O were added in the precursors and three batches of Fe$_2$O$_3$ QDs/FGS composites with theoretical Fe$_2$O$_3$/FGS mass ratios of 2:1, 1:1, and 1:2 were prepared. For comparison, bare Fe$_2$O$_3$ QDs were also prepared by the heat treatment of Fe(NO$_3$)$_3$·9H$_2$O at 200 °C for 10 h. To construct the asymmetric supercapacitors, the MnO$_2$/FGS composite with a MnO$_2$/FGS mass ratio of 2:1 was prepared by a similar method using Mn(NO$_3$)$_2$·9H$_2$O and FGS.

Materials Characterization: The crystallographic information and phase purity of the products were investigated by XRD (Shimadzu X-ray diffractormeter 6000, Cu *Kα* radiation), Raman spectroscopy (Jobin-Yvon T6400 micro-Raman system). The morphology and microstructure of the products were investigated by FESEM (Hitachi S4300), TEM (FEI-Philips CM300 UT/FEG), and HRTEM. N$_2$ adsorption–desorption isotherms were measured at the liquid nitrogen temperature using a Micromeritics ASAP 2010 instrument. The precise carbon contents in different composites were determined by TGA (Shimadzu DTG-60H). FTIR spectrum of the pristine FGS was collected from 4000 to 500 cm^{-1} using a Nicolet-670 FTIR spectrometer.

Electrochemical Measurements: To prepare the electrodes for electrochemical measurements, 80 wt% active material (Fe$_2$O$_3$/FGS, FGS, Fe$_2$O$_3$, and MnO$_2$/FGS), 10 wt% carbon black, and 10 wt% polyvinylidene difluoride dissolved in *N*-methylpyrrolidone were mixed to form a slurry. The slurry was pasted on Ti foil and dried in an electric oven at 80 °C for 12 h. The mass loadings for both Fe$_2$O$_3$/FGS and MnO$_2$/FGS electrodes are in the range of ≈2–3 mg cm^{-2}. The electrochemical tests of individual electrodes (Fe$_2$O$_3$/FGS, FGS, Fe$_2$O$_3$, or MnO$_2$/FGS) were performed using three-electrode cells with

www.MaterialsViews.com

ADVANCED
FUNCTIONAL
MATERIALS
www.afm-journal.de

FULL PAPER

a platinum foil counter electrode and an Ag/AgCl reference electrode. An asymmetric supercapacitor with Fe_2O_3/FGS anode and MnO_2/FGS cathode was assembled in Swagelok cell using porous nonwoven fabric as the separator. For both three-electrode cells and two-electrode cells, 1 M Na_2SO_4 was used as the electrolyte. CV and EIS measurements of different electrodes were measured using a CHI660D electrochemical workstation. Galvanostatic charge/discharge measurements were carried out on a battery testing system LAND CT2001A.

Supporting Information

Supporting Information is available from the Wiley Online Library or from the author.

Acknowledgements

[1] J. Jiang, Y. Y. Li, J. P. Liu, X. T. Huang, C. Z. Yuan, X. W. Lou, *Adv. Mater.* **2012**, *24*, 5166.
[2] C. Liu, F. Li, L. P. Ma, H. M. Chen, *Adv. Mater.* **2010**, *22*, E28.
[3] M. B. Zheng, J. Cao, S. T. Liao, J. S. Liu, H. Q. Chen, Y. Zhao, W. J. Dai, G. B. Ji, J. M. Cao, J. Tao, *J. Phys. Chem. C* **2009**, *113*, 3887.
[4] H. Pang, Y. Liu, J. Li, Y. Ma, G. Li, Y. Ai, J. Chen, J. Zhang, H. Zheng, *Nanoscale* **2012**, *5*, 503.
[5] H. Pang, Z. Yan, W. Wang, J. Chen, J. Zhang, H. Zheng, *Nanoscale* **2012**, *4*, 5946.
[6] J. T. Zhang, J. W. Jiang, H. L. Li, X. S. Zhao, *Energy Environ. Sci.* **2011**, *4*, 4009.
[7] Y. W. Cheng, H. B. Zhang, S. T. Lu, C. V. Varanasi, J. Liu, *Nanoscale* **2013**, *5*, 1067.
[8] B. Li, Y. S. Fu, H. Xia, X. Wang, *Mater. Lett.* **2014**, *122*, 193.
[9] J. Yan, A. Sumboja, X. Wang, C. P. Fu, V. Kumar, P. S. Lee, *Small* **2014**, *10*, 3568.
[10] Z. N. Yu, B. Duong, D. Abbitt, J. Thomas, *Adv. Mater.* **2013**, *25*, 3302.
[11] X. H. Xia, D. L. Chao, Z. X. Fan, C. Guan, X. H. Cao, H. Zhang, H. J. Fan, *Nano Lett.* **2014**, *14*, 1651.
[12] X. Zhao, C. Johnston, P. S. Grant, *J. Mater. Chem.* **2009**, *19*, 8755.
[13] W. Tang, L. L. Liu, S. Tian, L. Li, Y. B. Yue, Y. P. Wu, K. Zhu, *Chem. Comm.* **2011**, *47*, 10058.
[14] Q. T. Qu, Y. S. Zhu, X. W. Gao, Y. P. Wu, *Adv. Energy Mater.* **2012**, *2*, 950.
[15] X. H. Lu, M. H. Yu, T. Zhai, G. M. Wang, S. L. Xie, T. Y. Liu, C. L. Liang, Y. X. Tong, Y. Li, *Nano Lett.* **2013**, *13*, 2628.
[16] H. Xia, Y. S. Meng, G. L. Yuan, C. Cui, L. Lu, *Electrochem. Solid-State Lett.* **2012**, *15*, A60.
[17] D. S. Yuan, J. H. Zeng, N. Kristian, Y. Wang, X. Wang, *Electrochem. Commun.* **2009**, *11*, 313.
[18] R. Z. Li, J. P. Liu, *Electrochim. Acta* **2014**, *120*, 52.
[19] S. Chen, W. Xing, J. J. Duan, X. J. Hu, S. Z. Qiao, *J. Mater. Chem. A* **2013**, *1*, 2941.
[20] G. Binitha, M. S. Soumya, A. A. Madhavan, P. Praveen, A. Balakrishnan, K. R. V. Subramanian, M. V. Reddy, S. V. Nair, A. S. Nair, N. Sivakumar, *J. Mater. Chem. A* **2013**, *1*, 11698.
[21] X. H. Lu, Y. X. Zeng, M. H. Yu, T. Zhai, C. L. Liang, S. L. Xie, M. S. Balogun, Y. X. Tong, *Adv. Mater.* **2014**, *26*, 3148.
[22] X. H. Lu, M. H. Yu, G. M. Wang, Y. X. Tong, Y. Li, *Energy Environ. Sci.* **2014**, *7*, 2160.
[23] X. Zhao, C. Johnston, P. S. Grant, *J. Mater. Chem.* **2009**, *19*, 8755.
[24] Y. Li, L. T. Kang, G. L. Bai, P. Y. Li, J. C. Deng, X. G. Liu, Y. Z. Yang, F. Gao, W. Liang, *Electrochim. Acta* **2014**, *134*, 67.
[25] K. K. Lee, S. Deng, H. M. Fan, S. Mhaisalkar, H. R. Tan, E. S. Tok, K. P. Loh, W. S. Chin, C. H. Sow, *Nanoscale* **2012**, *4*, 2958.
[26] H. W. Wang, Z. J. Xu, H. Yi, H. G. Wei, Z. H. Guo, X. F. Wang, *Nano Energy* **2014**, *7*, 86.
[27] S. H. Yang, X. F. Song, P. Zhang, J. Sun, L. Gao, *Small* **2014**, *10*, 2270.
[28] R. W. Mo, Z. Y. Lei, K. N. Sun, D. Rooney, *Adv. Mater.* **2014**, *26*, 2084.
[29] C. X. Peng, B. D. Chen, Y. Qin, S. H. Yang, C. Z. Li, Y. H. Zuo, S. Y. Liu, J. H. Yang, *ACS Nano* **2012**, *6*, 1074.
[30] M. B. Zheng, D. F. Qiu, B. Zhao, L. Y. Ma, X. R. Wang, Z. X. Lin, L. J. Pan, Y. D. Zheng, Y. Shi, *RSC Adv.* **2013**, *3*, 699.
[31] H. Xia, Y. H. Wan, G. L. Yuan, Y. S. Fu, X. Wang, *J. Power Sources* **2013**, *241*, 486.
[32] M. S. Wu, R. H. Lee, J. J. Jow, W. D. Yang, C. Y. Hsieh, B. J. Weng, *Electrochem. Solid-State Lett.* **2009**, *12*, A1.
[33] K. Y. Xie, J. Li, Y. Q. Lai, W. Lu, Z. A. Zhang, Y. X. Liu, L. M. Zhou, H. T. Huang, *Electrochem. Commun.* **2011**, *13*, 657.
[34] J. C. Huang, S. N. Yang, Y. Xu, X. B. Zhou, X. Jiang, N. N. Shi, D. X. Cao, J. L. Yin, G. L. Wang, *J. Electroanal. Chem.* **2014**, *713*, 98.
[35] Z. Wang, C. Y. Ma, H. L. Wang, Z. H. Liu, Z. P. Hao, *J. Alloys Compd.* **2013**, *552*, 486.
[36] Y. Lin, X. Y. Wang, G. Qian, J. J. Watkins, *Chem. Mater.* **2014**, *26*, 2128.
[37] S. Shivakumara, T. R. Penki, N. Munichandraiah, *ECS Electrochem. Lett.* **2013**, *2*, A60.
[38] G. Q. Han, Y. Liu, L. L. Zhang, E. Kan, S. P. Zhang, J. Tang, W. H. Tang, *Sci. Rep.* **2014**, *4*, 4824.
[39] H. Xia, M. O. Lai, L. Lu, *J. Mater. Chem.* **2010**, *20*, 6896.
[40] Z. J. Fan, J. Yan, T. Wei, L. J. Zhi, G. Q. Ning, T. Y. Li, F. Wei, *Adv. Funct. Mater.* **2011**, *21*, 2366.
[41] V. Khomenko, E. Raymundo-Piñero, F. Béguin, *J. Power Sources* **2010**, *195*, 4234.
[42] T. Cottineau, M. Toupin, T. Delahaye, T. Brousse, D. Bélanger, *Appl. Phys. A* **2006**, *82*, 599.
[43] V. Khomenko, E. Raymundo-Piñero, E. Frackowiak, F. Béguin, *Appl. Phys. A* **2006**, *82*, 567.
[44] M. S. Hong, S. H. Lee, S. W. Kim, *Electrochem. Solid-State Lett.* **2002**, *5*, A227.
[45] W. H. Jin, G. T. Cao, J. Y. Sun, *J. Power Sources* **2008**, *175*, 686.
[46] W. S. Hummers, R. E. Offeman, *J. Am. Chem. Soc.* **1958**, *80*, 1339.
[47] Q. L. Du, M. B. Zheng, L. F. Zhang, Y. W. Wang, J. H. Chen, L. P. Xue, W. J. Dai, G. B. Ji, J. M. Cao, *Electrochim. Acta* **2010**, *55*, 3897.